Quantifying mantle mixing through configurational Entropy

Erik van der Wiel[1], Cedric Thieulot[1], Douwe J.J. van Hinsbergen[1]

[1] Department of Earth Sciences, Utrecht University, Princetonlaan 8A, 3584 CB Utrecht, the Netherlands

Corresponding author: e.vanderwiel@uu.nl

Abstract

Geodynamic models of mantle convection provide a powerful tool to obtain insights into the structure and composition of the Earth's mantle that resulted from a long history of differentiating and mixing. Comparing such models with geophysical and geochemical observations is challenging as these datasets often sample entirely different temporal and spatial scales. Here, we explore the use of configurational entropy, based on tracer and compositional distribution on a global and local scale. We show means to calculate configurational entropy in a 2D annulus and find that these calculations may be used to quantitatively compare long-term geodynamic models with each other. The entropy may be used to analyze, with a single measure, the mixed state of the mantle as a whole and may also be useful to validate numerical models against local anomalies in the mantle that may be inferred from seismological or geochemical observations.

1. Introduction

Mantle convection models that are used to simulate the evolution and dynamics of the solid Earth are stooled on different sets of observations each providing their own constraints to validate the state of the mantle through time (e.g., Dannberg & Gassmöller, 2018; Gerya, 2014). For instance, with the advent of full-plate kinematic reconstructions of the past 100s Ma (e.g., Domeier & Torsvik, 2014; Merdith et al., 2021), mantle models can now be driven by plate motions through geological time (e.g., Coltice & Shephard, 2018; Flament et al., 2022; Heister et al., 2017). Such experiments then lead to a prediction of the structure and composition of the mantle that may be compared to geological, geochemical, or seismological observations from the modern Earth (e.g. Bower et al., 2015; Flament et al., 2022; Li et al., 2023; Lin et al., 2022; Yan et al., 2020).

Key observables of the modern Earth that may be predicted by models are anomalies in mantle structure or composition that result from mantle mixing, or absence thereof. For instance, seismic tomography provides images of the present-day mantle as relative slow and fast regions in terms of seismic wave propagation, which can relate to variations in temperature and/or composition such as slabs or mantle plumes (Koelemeijer et al., 2017; Ritsema & Lekić, 2020). The heterogeneity of the Earth's mantle is also reflected in geochemical observations of magmatic rocks, oceanic island basalts (OIB) and mid-oceanic ridge basalt (MORB), which suggest the existence of depleted, enriched, and even primordial mantle reservoirs, i.e. unmixed regions that maintain a geochemically distinct composition (Jackson et al., 2018; Jackson & Macdonald, 2022; McNamara, 2019; Stracke et al., 2019). Notably, seismological and geochemical heterogeneities may entirely, partly, or hardly overlap, and observations may relate to entirely spatial and temporal scales. Seismology reveals seismic velocity anomalies in the mantle on scales of 100s to 1000s of km, varying from slabs to LLSVPs (e.g., Garnero et al., 2016; Ritsema et al., 2011; Van der Meer et al., 2018). Geochemical differences between MORBs from the Atlantic, Pacific and Indian Ocean indicate compositional heterogeneity on a hemispheric scale (Doucet et al., 2020; Dupré & Allègre, 1983; Hart, 1984; Jackson & Macdonald, 2022), geochemical zonation within a single plume system is evidence for heterogeneities on a 100 km scale (Gazel et al., 2018; Hoernle et al., 2000; Homrighausen et al., 2023; Weis et al., 2011), whereas micro-scale analysis reveals even major variations between samples (Stracke et al., 2019). All such variations may result from a cycle of geochemical differentiation and renewed mixing that is associated with mantle convection and that eventually may be predicted by mantle convection models. To this end it is important to be also able to define or quantify the mixed state of the modern mantle from a suitable numerical mantle convection model the relevant range of spatial scales.

Here, we investigate the merits of configurational (or 'Shannon') entropy for quantifying compositional mixing of particles through flow on a global or local scale (Camesasca et al., 2006; Naliboff & Kellogg, 2007; Shannon, 1948). We develop the application of configurational entropy to the 2D cylindrical mantle convection models which we recently developed (van der Wiel et al., 2023), implementing measures for local and global entropy of mixing that incorporates information on composition. We aim to use configurational entropy to quantify the degree of mixing on different scales for different hypothetical initial compositional configurations of the mantle and evolution thereof over time. Subsequently, we discuss how configurational entropy may be used as a bridge for quantitative comparison between mantle convection models and geological, seismological, or geochemical observations.

2. Methods

2.1. Mixing entropy

Configurational Entropy (Shannon, 1948) describes how fast information on compositional particle distribution is lost through flow. It is widely used and has a large variety of applications, including fluid or magma mixing (Camesasca et al., 2006; Naliboff & Kellogg, 2007; Perugini et al., 2015), transport of plastic in oceans (Wichmann et al., 2019), distribution of seismicity in earthquake populations (Goltz & Böse, 2002), or the quantification of uncertainty in geological models (Wellmann & Regenauer-Lieb, 2012).

The definition of the entropy S is based on the probability of a particle distribution in a domain tessellated by non-overlapping cells. For this we use passive particles, or tracers, that are advected in a flow model leading to particle trajectories. The entropy depends on the distribution of particles, the number of cells and the initial compositional distribution (see section 2.3). Let C be the number of compositions and M the number of cells in the domain. The entropy is calculated based on the discretized particle density $\rho_{c,j}$ (Eq. 1), i.e., the amount particles of composition *c* in cell *j*,

$$\rho_{c,j} = \frac{n_{c,j}}{N_c} \tag{1}$$

where N_c is the total number of c-particles divided by the number of cells M. This assumes that cells are of equal area, which will be used here in our 2D application. Hence, N_c is the same for all cells. From the compositional density $\rho_{c,j}$ we calculate the conditional probability $P_{j,c}$ for finding a group of particles of composition *c* in cell *j* through Eq. (2)

$$P_{j,c} = \frac{\rho_{c,j}}{\sum_{c=1}^{C} \rho_{c,j}} \tag{2}$$

and as well the probability for the cell-sum of compositional densities P_j by Eq. (3),

$$P_j = \frac{\sum_{c=1}^{C} \rho_{c,j}}{\sum_{j=1}^{M} \sum_{c=1}^{C} \rho_{c,j}} \tag{3}$$

Next, Eq. 4 defines the global entropy S_{pd} of the particle distribution.

$$S_{pd} = -\sum_{j=1}^{M} P_j \ln P_j \tag{4}$$

which quantifies the global spatial heterogeneity of the particle distribution independent of composition (Naliboff & Kellogg, 2007). At the cell level, the local entropy S_j for cell *j* can be defined for the mixture of particles with different compositions:

$$S_j = -\sum_{c=1}^{C} P_{j,c} \ln P_{j,c} \tag{5}$$

Finally, the global entropy S of the particle distribution, accounting for composition, is the weighted average of P_j (Eq. 3) and the local entropy S_j (Eq. 4) through Eq. (6) (Camesasca et al., 2006).

$$S = \sum_{j=1}^{M} P_j S_j \tag{6}$$

Maximum entropy is achieved when all particle densities $\rho_{c,j}$ are equal, i.e., the distribution of composition and number of particles are the same in each cell. Each entropy above has a different maximum which depends on either the number of cells for (S_{pd}) or the number of compositions used (for S and S_j). To compare entropies between mixing models with different initial conditions, we normalize the entropies by dividing each by its maximum. The maximum for S_{pd} is equal to $\ln M$, while for S_j and S the maximum is $\ln C$ (Camesasca et al., 2006). This provides values for all entropies between the endmembers 0 (entirely segregated composition) and 1 (uniformly mixed). The maximum value for S_{pd} can only be reached when all compositions are present in equal ratios. Entropy calculations of four simple educational examples are shown and explained in appendix A to help the reader appraise these quantities.

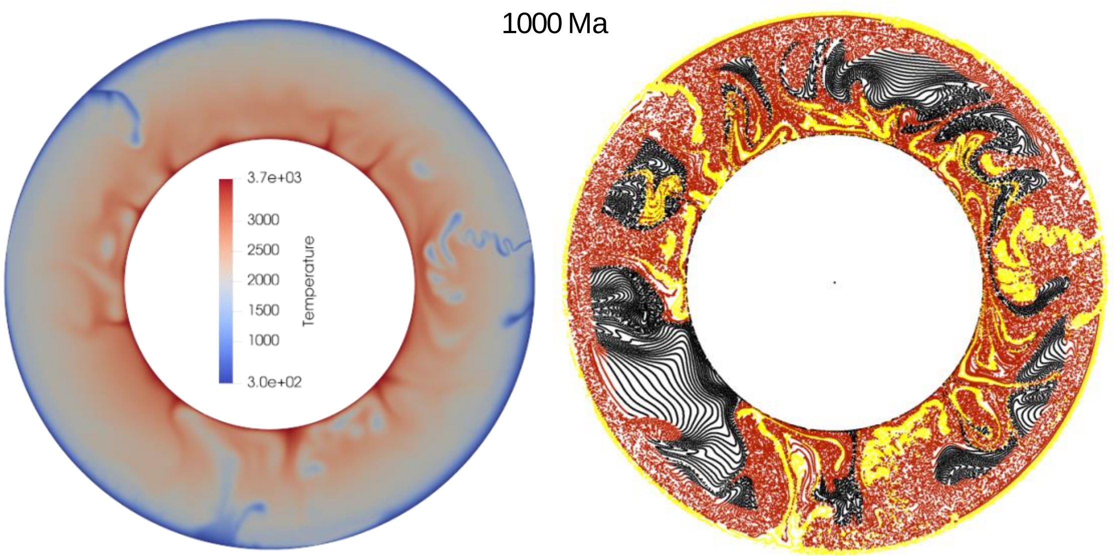

Figure 1 - Snapshot from model R at t=1000 Ma showing the temperature field in Kelvin (left) and passive particles colored by composition (lithosphere: yellow, upper mantle: red, lower mantle: black).

2.2 Mantle convection model

We apply the configurational entropy to the quantification of mixing in a recently developed 2D numerical mantle model in a 2D cylindrical geometry that simulates 1000 Ma of ongoing mantle convection and subduction (van der Wiel et al., 2023). The convection model was designed to evaluate the sensitivity of inferred lower mantle slab sinking rates (Van der Meer et al., 2018) to the vigor of mantle convection. The simulations comprised dynamically self-consistent one-sided subduction below freely moving, initially imposed, continents at the surface, culminating in slab detachment followed by sinking of slab remnants across the lower mantle (Fig. 1). Model plate motions were in the range of reconstructed values (Zahirovic et al., 2015) and average slab sinking rates could be obtained in the range of those that were inferred from correlations between the location of imaged lower mantle slabs and their geological age (Van der Meer et al., 2018). This modelling qualitatively illustrated the degree of mixing in a modelled mantle and the potential preservation of an unmixed primordial, unmixed advected (e.g., subducted), or (partly) homogenized, mixed mantle shown by the distribution of particles.

We quantify the degree of mantle mixing in the model by investigating the local and global mixing entropies (Section 2.1) for model *R* of van der Wiel et al. (2023) at different resolutions. We also illustrate how mixing entropy quantifies the mixing of a different model (model P) that showed significantly higher slab sinking rates than inferred for the lower mantle and that displayed a higher degree of mantle mixing (van der Wiel et al., 2023). For this purpose, we only used the passive particle distribution available from the models in van der Wiel et al., 2023. The cells used to calculate the configurational entropy (see section 2.4) are independently substantiated and therefore not the same as used in the numerical model, for any additional information of these models we refer the reader to van der Wiel et al., 2023.

2.3 Initial composition

To illustrate how we track compositional evolution with configurational entropy, we assign a compositional distribution to our example models with two different approaches. In case A, we assign a compositional distribution in the initial model, and each tracer will keep its initial composition through time. We divide the annulus in two concentric parts at a radius of 5100 km and assign the inner and outer part a different composition (simply put: a different color). This creates a 50-50 ratio between the number of particles of each composition. Case B uses dynamic compositions, i.e., the composition of a particle may change over time. We use three compositions whose relative ratios are allowed to change over time depending on the particle's depth in the model. Initially, we define particles as lower mantle when they start below 660 km depth in the model, upper mantle if they start between 100 and 660 km, and lithosphere if between 0 and 100 km depth. Particles keep their 'lower mantle' composition as long as they do not ascent above the 660 km during model evolution. Any particle that moves from a deeper reservoir into a shallower will change its composition to the shallower reservoir and will maintain this composition for the remainder of model time. This approach is an example that may be used in a study to characterize the secular geochemical differentiation of the solid Earth.

2.4 Cell distribution

Entropy as calculated in this study also depends on the number and distribution of cells, which is independent of the mesh used in the numerical model itself. To ensure an approximately equal cell-area throughout our domain, we vary the number of cells per radial layer. The cell-area is determined by the product of the radial extent δr and lateral extent $\delta\theta$ that follows from the number of radial layers and the number of cells along the core-mantle-boundary (CMB) circumference. Varying cell-area may be important to compare the outcome of a numerical model with datasets that have very different resolutions (e.g., seismology versus geochemistry). We illustrate different cell resolutions with our 2D example model, but a similar approach may be used for a 3D model albeit with a different tessellation (Thieulot, 2018). The lowest resolution (10x40) contains 40 cells along the CMB, increasing across the 10 layers to 68 cells along the surface, for a global total of 539 cells (Fig. 2). The highest resolution that we illustrate (20x160) then gives a global total of 4430 cells (Fig. 2). The numerator $\rho_{c,j}$ for the probability calculations (Eq's 2 & 3) for cells that do not contain a particle ($\sum_{c=1}^{C} \rho_{c,j} = 0$) would contribute to the entropy via the natural logarithm. Note that $\lim_{x \to 0} x \ln x = 0$ and therefore cells without a particle do not add to any of the entropies and are skipped in practice in the summation of Eq's (4-6).

3. Results

In this section, we describe the various obtained entropies. Starting with the particle distribution $S_{pd.}$ Next, we underline the importance of resolution for the local entropy S_j in our example model at different resolutions for the static composition distribution (case A) and show how the local entropy evolves over time. Finally, we show the temporal evolution of the global entropy S for this model, which is also influenced by resolution and compositional choices before we elaborate on the use of dynamic compositions (case B, section 3.4).

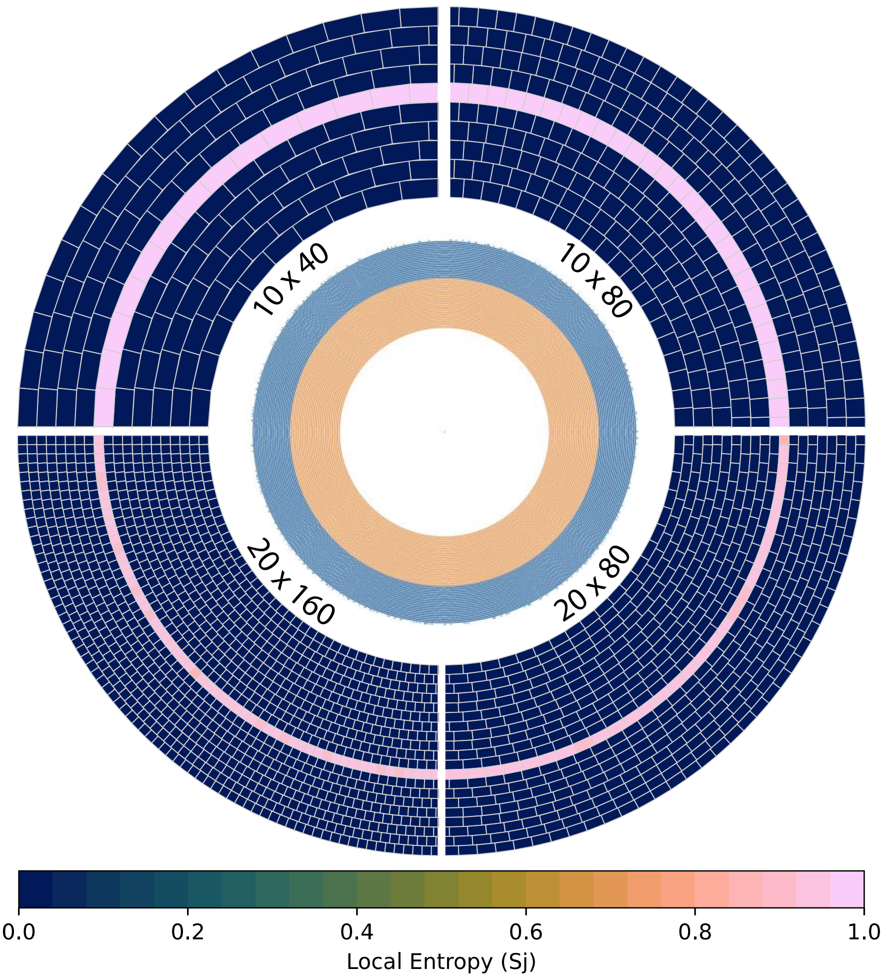

Figure 2: Representation of the various tested resolutions. Shown is the initial (t=0 Ma) particle distribution (inner annulus) and local entropy S_j (outer annulus) for the static 50/50 composition distribution (case A). The cells with a high S_j (pink) indicate that both compositions are present, the unmixed cells (blue) contain only one composition.

3.1 Global particle distribution (S_{pd})

A total of ~96,000 of particles are initially distributed in a regular pattern (Fig. 2), equally spaced throughout the annulus. Over time, these particles are passively advected and their spatial distribution thus changes. The large number of particles in the initial distribution provides a good coverage in all cells as quantified by the normalized global entropy of particle distribution S_{pd} which is at the modelling start close to 1 for both cases A & B at the start (Fig. 3). As the initial composition ratios of case B are not equal (about 72% lower mantle, 25% upper mantle, and 3% lithosphere) S_{pd} is not 1 as for case A, but ~0.95, still indicating that particles are distributed equally.

Over time, as particles are advected, the S_{pd} does not change significantly for case A in which particles cannot change composition, but it does change for case B (Fig. 3). This is caused by the secular change in composition ratios in case B (Fig. 8 of van der Wiel et al., 2023). S_{pd} increases due to the increased percentage of lithosphere and upper mantle particles in the domain. We tested the effect of cell resolution on S_{pd} for both cases, which does not show significant differences (Fig. 3). This indicates that the number of particles used in our calculations is sufficient, also for our highest resolution (20x160).

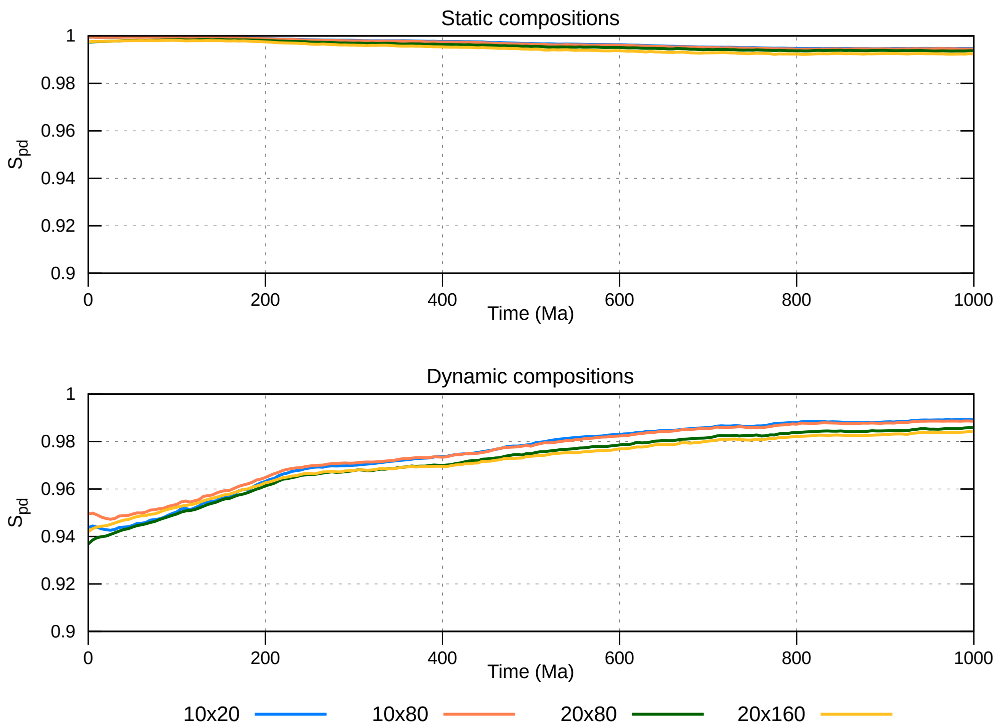

Figure 3: Time evolution of S_{pd} for the static (case A) and dynamic (case B) composition distributions of the four used resolutions.

3.2 Local entropy (S_j)

A local entropy of 1 means that the ratio of particle compositions within a cell is equal to the global composition ratio, i.e., in the initial distribution for case A (Fig. 2). $S_j = 0$ indicates that all particles in a cell have the same composition, although, it does not indicate which composition. We illustrate the temporal evolution of particle distribution in 250 Ma steps (Fig. 4) for which we use the static particle composition ratio of case A and a cell resolution of 10x80 at the CMB (Fig. 3). After 250 Ma of convection evolution the initial distribution is undisturbed in most parts of the domain. The two compositions are only displaced since the onset of convection, but barely mixed. Mixing is concentrated around two major zones of downwelling where a narrow zone of single cells shows a local entropy S_j that is non-zero (Fig. 4a).

At 500 Ma, some of the sharp boundaries between the two compositions have moved and a mixed boundary zone formed locally, reflected by the broader zone of non-zero local entropy (Fig. 4b). After 750 Ma, most of the upper mantle (top three cells) has $S_j > 0$ and zones in the lower mantle are mixed as well (Fig. 4c): the two starting compositions have been displaced and mixed through the mantle. At the end of the model, at 1000 Ma, the number of cells with non-zero S_j in the upper mantle has decreased further, the zones of fully ($S_j \approx 1$) mixed lower mantle have increased in area. However, there are still zones of unmixed ($S_j = 0$) composition present. Unmixed initial 'lower' composition is preserved mainly in the mid-mantle while unmixed initial 'upper' composition is preserved near the CMB, i.e., this material sunk and was displaced, but did not mix (Fig. 4d).

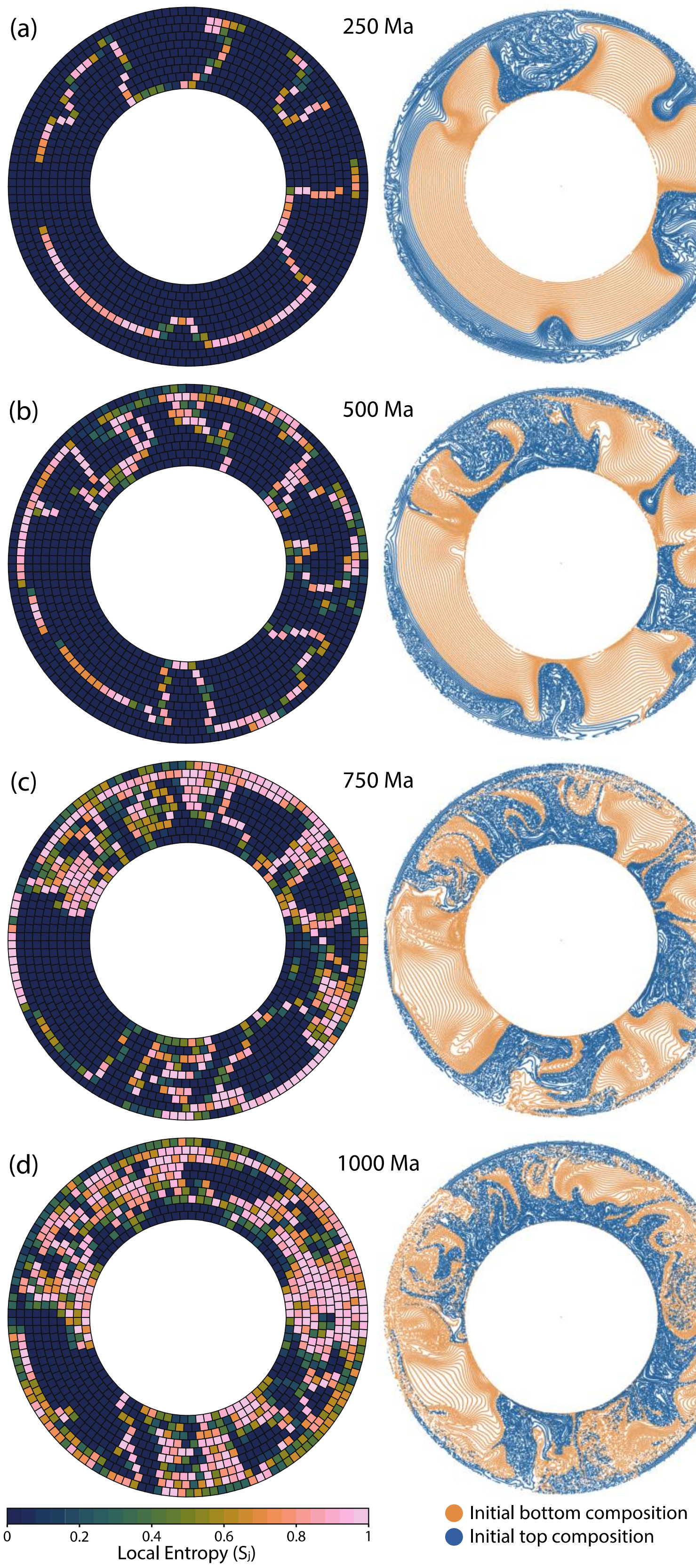

Figure 4 - Local Entropy S_j (left) and particle distribution (right) at 250 Ma intervals of the model (model R - van der Wiel et al., 2023) with a static 50/50 ratio particle composition (case A) at a resolution of 10x80 cells.

Even though cell resolution does not significantly impact S_{pd} it does affect the local entropy S_j (and thus also the global entropy, see next section). A smaller-sized cell mesh will have fewer particles per cell, which increases the likelihood of sampling particles of only one composition in zones with limited mixing, leading to zero local entropy. Doubling the angular resolution from 10x40 to 10x80 shows on a global scale a similar trend after 1000 Ma of convection: three zones of unmixed (low S_j) mantle separated by three zones of mixed mantle (high S_j) (Fig. 5). However, it does show some increased detail in local entropy, mainly in the 'mixed' zones of the model (Fig. 5). The large unmixed zones are of similar size for these two resolutions, although the ratio of cells with a low S_j compared to high S_j changed. The larger unmixed zones are composed of initial 'lower' composition (Fig. 4d).

A radial increase in resolution, from 10 to 20 cells across the domain, refines the calculation of local entropy. The number of cells with $S_j = 0$ becomes larger and increases the size of the three main unmixed zones. At this resolution, S_j resolves the 'continents': thicker portions of lithosphere that were initially placed in the model (See Fig 2. of van der Wiel et al., 2023). The 20x80 resolution has unmixed cells in regions that had high S_j at lower resolutions (Fig. 5). Finally, with the 20x160 mesh resolution, zones of initial upper and lower composition (Fig. 4d) show up as low S_j bounded by a single line of cells with high S_j (Fig. 5). At this resolution the local entropy calculation resolves mantle structures such as the boundaries between slabs and ambient mantle, showing mantle structure mapped into the local entropy of mixing.

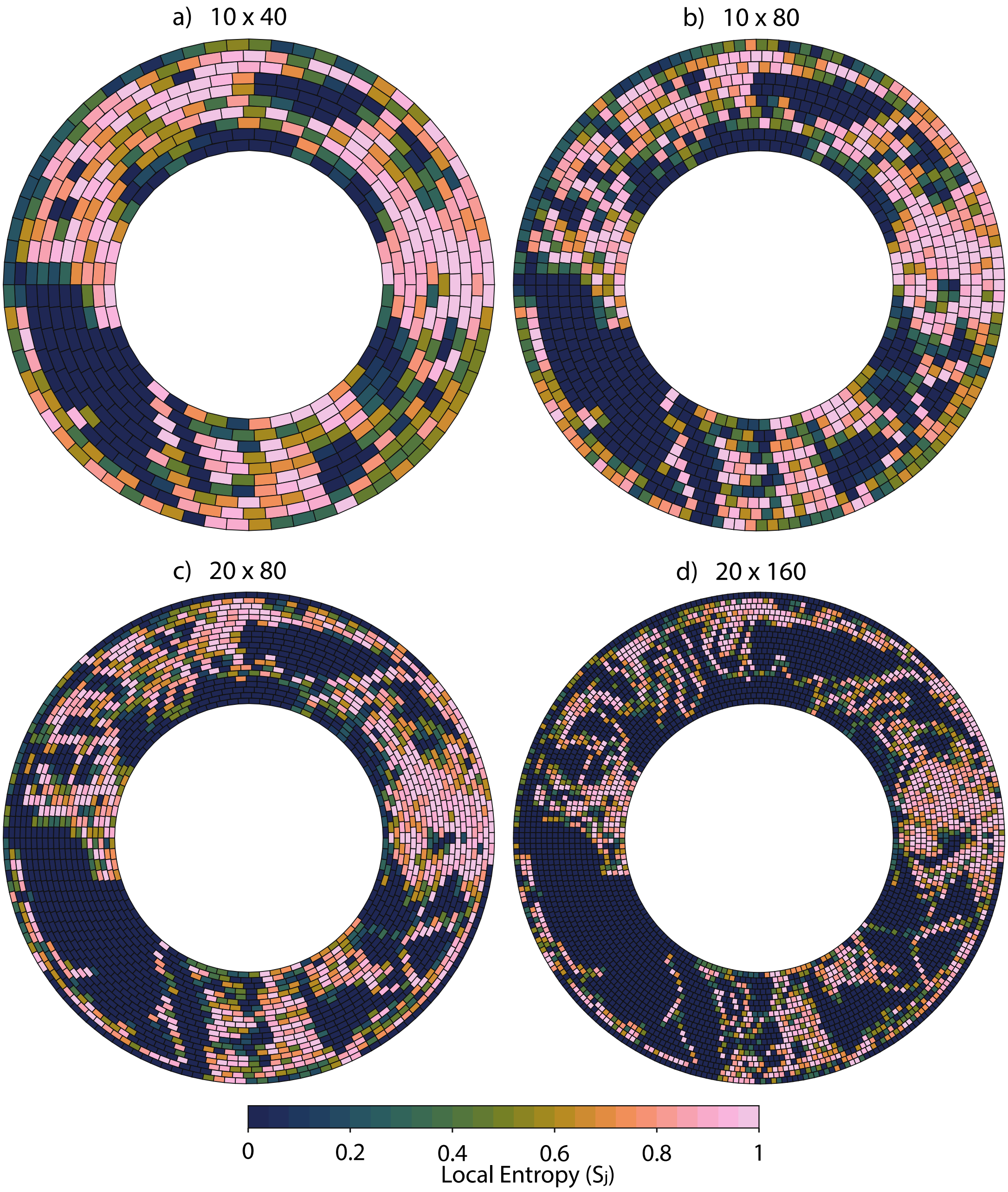

Figure 5 - Local Entropy S_j after 1000 Ma of mantle convection for the Reference model (van der Wiel et al., 2023) at four different resolutions of cells used to calculate the local entropy where b is identical as figure 4d.

3.3 Global entropy (S)

The global entropy is a weighted average of the particle distribution probability P_j over cells and the compositional distribution within the cells S_j (Eq. 6). Because the particle distribution irrespective of composition is almost equal to 1 in all tests (Fig. 2, section 3.1), we may consider the entropy S as proxy for global compositional mixing. For the initial distribution of composition based on depth, almost all cells have a local entropy $S_j = 0$, apart from the cells that straddle the compositional boundary (Fig. 2). This distribution is an unmixed state of the mantle and has a low global entropy, $S = 0.1$ for the resolutions with 10 radial levels and $S = 0.06$ for those with 20 radial levels (Fig. 6). The spherical resolution does not matter for the initial distribution as the ratio of non-zero to zero S_j cells is the same.

While the mantle flow model evolves, compositions become more mixed and the global entropy increases depending on mesh resolution, whereby smaller cells have a higher probability to sample only one composition. Therefore, a higher resolution (smaller cells) yields a lower global entropy after 1000 Ma of mantle convection: the 20x160 resolution yields $S = 0.32$ while the 10x40 resolution yields $S = 0.51$ (Fig. 6).

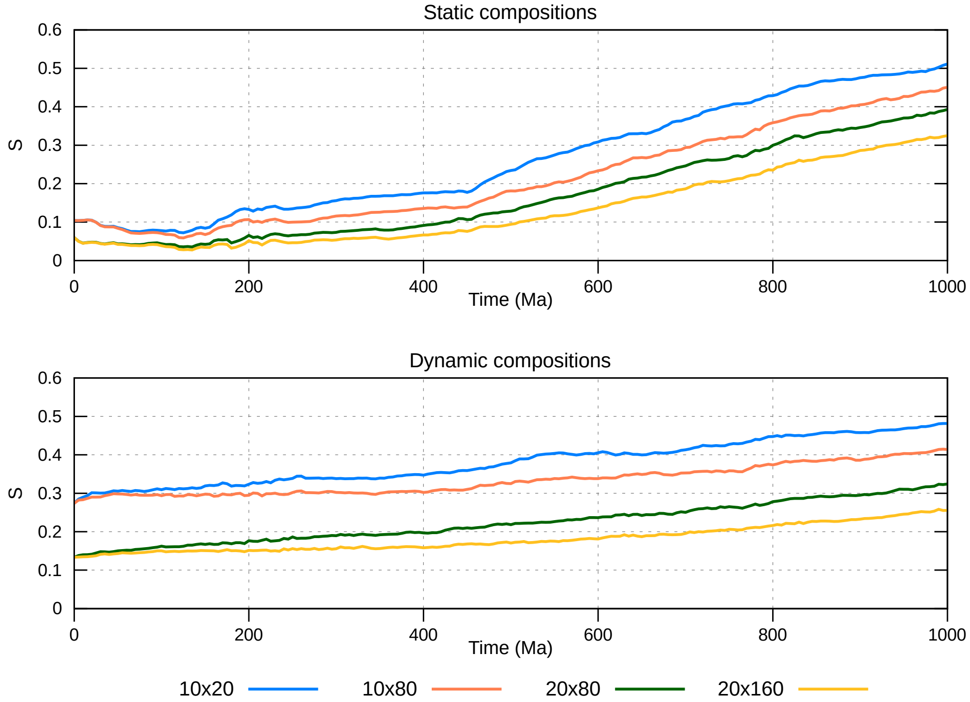

Figure 6 - Global Entropy S of the model through time for different cell resolutions. Top: Case A (static compositions, bottom: case B (dynamic compositions).

3.4 Case study: entropy with dynamic compositions

Case B, which has dynamic compositions that depend on compositional evolution in the model, presents a practical application of the configurational Entropy. We track the entropy as the compositional ratios evolve and mix over time. The total number of particles that have been part of the lithosphere and subducted increases over time as new lithosphere and slab is being created while the volume of material that has stays in the lower mantle decreases. In our example model, after 1000 Ma, the initial volumes of 3% lithosphere, 25% upper mantle, and 72% lower mantle have changed to 25% with lithosphere ‘composition’, 50% upper mantle and 25% lower mantle. In this example, the dynamic composition implies that no lower mantle composition exists above the 660 km-discontinuity and therefore cannot have a local entropy of 1. However, in parts of the lower mantle the three compositions are mixed where high local entropy is present. The parts of the domain containing subducted lithosphere are better mixed, indicative of the convective mixing behavior of our model. With the highest mesh resolution we can resolve the upper-to lower-mantle boundary in the local entropy as well as active and past locations of subduction (Fig. 7a).

The unmixed zones are of particular interest since they may provide direct information about compositions after 1000 Ma of convection. For all compositions there are cells with an unmixed signal, revealing the state of preservation of these compositions over time and over the whole domain. The entropy figures illustrate for instance, the survival of unmixed ‘primordial’ lower mantle material in the model, the fate of subducted lithosphere, and how upper mantle material is entrained downward during subduction (Fig. 7a).

This case has an entirely different local entropy than the static composition distribution of case A (Fig. 5). The dynamic case mainly focusses on the fate of subducted lithosphere rather than global mixing of the upper and lower part of the domain. As in the example with a static composition (case A), the global entropy S for dynamic compositions is also cell-size-dependent. The initial global entropy is higher than for static compositions as there are now two compositional boundaries and over time the entropy only increases up to $S = 0.25$ for the 20x160 resolution. For the 10x40 resolution, $S = 0.48$ after 1000 Ma which is in the same range as the static two-composition example (Fig. 6).

Finally, we use the dynamic composition to illustrate how changing the vigor of mantle convection changes the entropy. To this end, we compute the entropy after 1000 Ma using a model in which much higher sinking rates of subducted slabs occurred than inferred (model P - van der Wiel et al., 2023) and that consequently has faster mantle flow. Fig. 7b illustrates that this model is much more mixed after 1000 Ma of convection than in model R (Fig. 7a). It has cells with a local entropy close to 1 throughout much of the domain, unmixed zones are smaller and located only in the top of lower mantle. Most of the local entropies are in the mid-mixed range. This is because only 10% of the original 'lower mantle' composition remains. global entropy $S = 0.42$ for this model at the 20x160 resolution, and even 0.60 for the 10x40 resolution, significantly higher than the reference model with dynamic composition (Fig. 6). This example illustrates that the configurational entropy successfully quantifies mixing states and are sensitive to overall changes in model behavior.

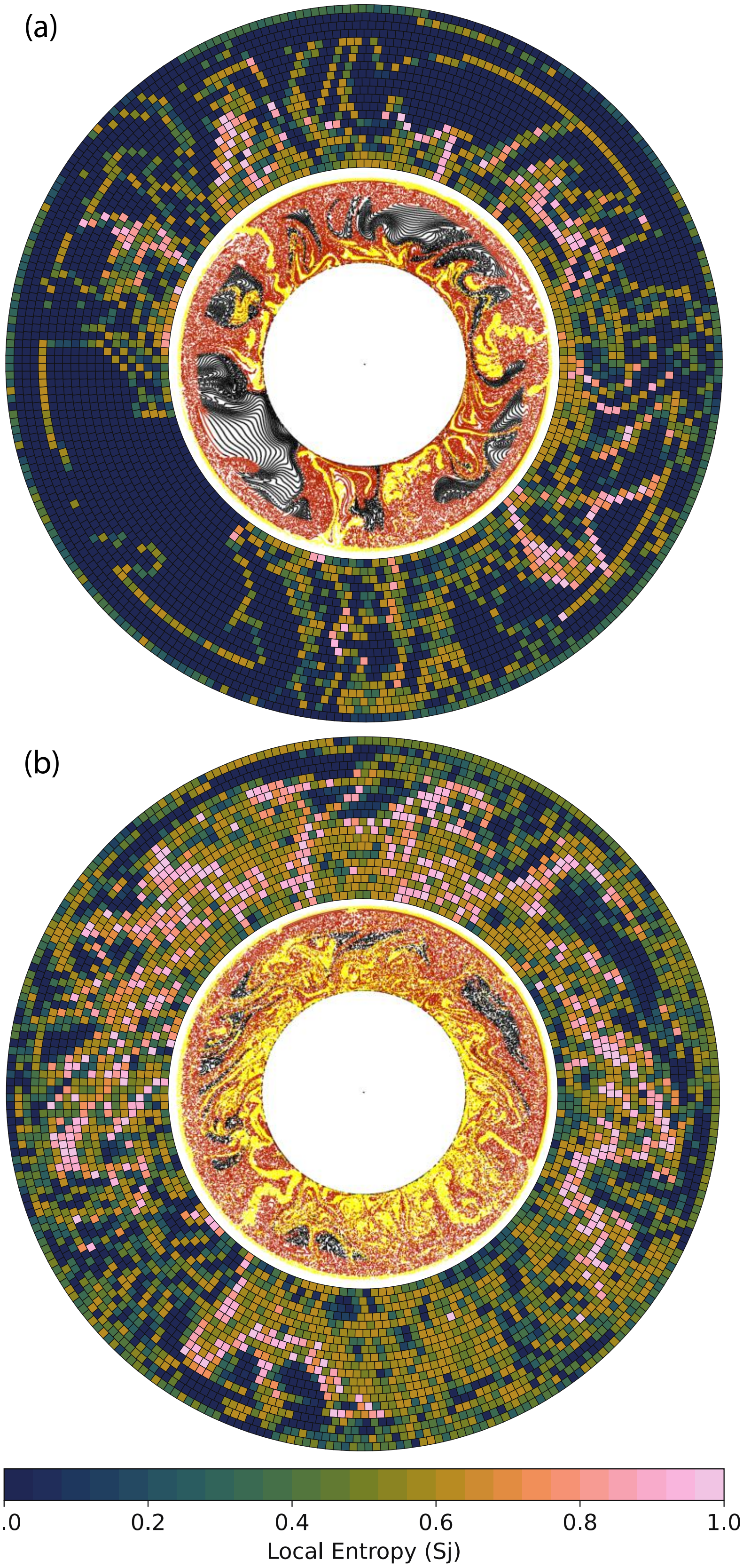

Figure 7 - Local Entropy S_j with a 20x160 resolution (outer annulus) and particle distribution (inner annulus) for dynamic compositions. Lower mantle (black), upper mantle (red) and lithosphere (yellow) compositions can change over time as function of depth. a) model R and b) model P with more vigorous convection of van der Wiel et al., (2023) as described in section 3.4.

4. Outlook and conclusion

In this paper, we explore how configurational entropy may be applied to mantle convection models to quantify the degree of mechanical mixing, both on a local and global scale. Our results illustrate that entropy provides a way to track or map compositional heterogeneity over time using tracers or particles, which are commonly available in geodynamical models. Depending on the complexity of numerical models, any information that is stored on these tracers can be used to differentiate between 'compositions' used in the entropy calculations. The mantle convection models that we used to illustrate the use of configurational entropy were designed as numerical experiments to evaluate whether slab sinking rates scale with the vigor of mantle convection and mixing and did not aim to make a direct comparison between model and the real Earth. However, for models that do, i.e. kinematically constrained by reconstructed plate motions and aiming to resemble Earth-like features (e.g., Bull et al., 2014; Coltice & Shephard, 2018; Faccenna et al., 2013; Flament et al., 2022; Li et al., 2023; Lin et al., 2022) configurational entropy may serve as a means to quantify and map the degree of mixing, and hence to determine average cell composition, on a local, regional or a global scale.

On a global scale, such models would for instance be able to track volumes of material that have remained in the lower mantle during the evolution of Earth (Fig. 7). These volumes are of interest, because they could explain the geochemical detection of enigmatic primordial mantle, and feature in numerical models as the proposed bridgemanite-enriched ancient mantle structures (BEAMS) of (Ballmer et al., 2017), or surviving in the slab graveyard (Jones et al., 2021), or perhaps in LLSVPs or ULVZs (Deschamps et al., 2012; Flament et al., 2022; McNamara, 2019; Vilella et al., 2021). In addition, the use of entropy calculations may show how subducted lithosphere may become stored in the mantle and to what degree original depleted and enriched crust, and slab material mix with upper and lower mantle rock. Particularly, dynamically changing compositions would benefit such studies, and in more sophisticated models that include geochemical evolution (e.g., Dannberg & Gassmöller, 2018; Gülcher et al., 2021), geochemical reservoirs can be quantified with configurational entropy.

At smaller scales, entropy in mantle modeling is useful to track mixing at the scale of a single subducting plate interacting with a mantle wedge, or a plume rising from the CMB. This may be done based on location solely (S_{pd}), to track the dispersal of an initial cloud of tracers in a slab or at the base of a plume (Naliboff & Kellogg, 2007), but also with the use of composition through S_j and S. For instance, it may quantify how different compositions of material from the lowermost mantle are entrained by a plume and how material entrained by that plume is mixed during its upward motion (e.g., Dannberg & Gassmöller, 2018). For instance, how material is mixed in the partially melting plume head, or in the partially melting upper mantle below a ridge, mixing on the scale of a magma chamber may also be mapped using configurational entropy, see (Perugini et al., 2015).

However, it may not yet be possible to numerically represent 3D mixing and motion processes on all the scales illustrated above. In the end, the dynamics driving mantle convection may force slow consumption and mixing away of primordial mantle by producing lithosphere and plumes and mixing the geochemically segregated remains of these back into the mantle. These processes lie at the basis for the widely recognized but still enigmatic geochemical reservoirs that are thought to reside in the lower mantle such as those of recycled continental crust (EM1, EM2), recycled oceanic crust (HIMU) (Yan et al., 2020), recycled depleted lithospheric mantle (Stracke et al., 2019), and remaining primordial mantle (Ballmer et al., 2017; Gülcher et al., 2020; Jackson et al., 2017). These processes also culminate in the seismologically imaged mantle volumes of higher and lower seismic velocity, or seismic attenuation, but the widely different scales at which geochemical and seismological observations are made poses a problem to link such observations. Numerical models may bridge these scales and eventually use our planets plate tectonic evolution to predict the geochemical reservoirs as tapped by volcanoes, and mantle structure as imaged by seismology. The configurational entropy in this paper may be helpful to quantitatively determine where numerical models may successfully predict these seismological and geochemical features.

Appendix A

We here recall the equations of the manuscript and show the equations for normalization.

$$\rho_{c,j} = \frac{n_{c,j}}{N_c} \tag{1}$$

$$P_{j,c} = \frac{\rho_{c,j}}{\sum_{c=1}^{C} \rho_{c,j}} \tag{2}$$

$$P_j = \frac{\sum_{c=1}^{C} \rho_{c,j}}{\sum_{j=1}^{M} \sum_{c=1}^{C} \rho_{c,j}} \tag{3}$$

$$S_{pd} = -\sum_{j=1}^{M} P_j \ln P_j \tag{4}$$

$$S_j = -\sum_{c=1}^{C} P_{j,c} \ln P_{j,c} \tag{5}$$

$$S = \sum_{j=1}^{M} P_j S_j \tag{6}$$

$$S_{pd\ normalized} = \frac{S_{pd}}{\ln M} \tag{7}$$

$$S_{j\ normalized} = \frac{S_j}{\ln C} \tag{8}$$

$$S_{normalized} = \frac{S}{\ln C} \tag{9}$$

Four examples are given below, each with different distributions of particles and compositions in a small rectangular grid of 4 cells. We use these four examples to illustrate how the configurational entropy is affected by certain distributions. The background of the cells is colored according to S_j in grayscale, from 0 (black) to 1 (white) and the tracers shown are randomly given a position in the cell appointed to them.

Example 1 – equal distribution, fully mixed

We start with a uniform distribution of particles with completely mixed compositions in each cell. The number of expected particles per composition per cell (N_c) is equal to the sum of the number of particles in that cell, this also reflected in vector P_j which is equal for all cells – and therefore S_{pd} is equal to 1 (after normalization) indicating a uniform distribution. The local entropy S_j per cell is defined through $P_{j,c}$ which is equally distributed and equal to the normalization. Therefore, it indicates perfect mixing for all four cells. The global entropy combines P_j and S_j and is therefore equal to the endmember, which is 1.

$$n_{c,j} = \begin{pmatrix} 3 & 3 & 3 & 3 \\ 3 & 3 & 3 & 3 \end{pmatrix}$$

$$N_c = \begin{pmatrix} 3 \\ 3 \end{pmatrix}$$

$$\rho_{c,j} = \begin{pmatrix} 1 & 1 & 1 & 1 \\ 1 & 1 & 1 & 1 \end{pmatrix}$$

$$P_{j,c} = \begin{pmatrix} 1/2 & 1/2 & 1/2 & 1/2 \\ 1/2 & 1/2 & 1/2 & 1/2 \end{pmatrix}$$

$$P_j = (1/4 \;\; 1/4 \;\; 1/4 \;\; 1/4)$$

$$S_{pd} = 1.38629$$

$$S_j = (0.693 \;\; 0.693 \;\; 0.693 \;\; 0.693)$$

$$S = 0.69314$$

$$S_{pd\ normalized} = \frac{1.38629}{\ln 4} = 1$$

$$S_{j\ normalized} = (1\ 1\ 1\ 1)$$

$$S_{normalized} = \frac{0.69314}{\ln 2} = 1$$

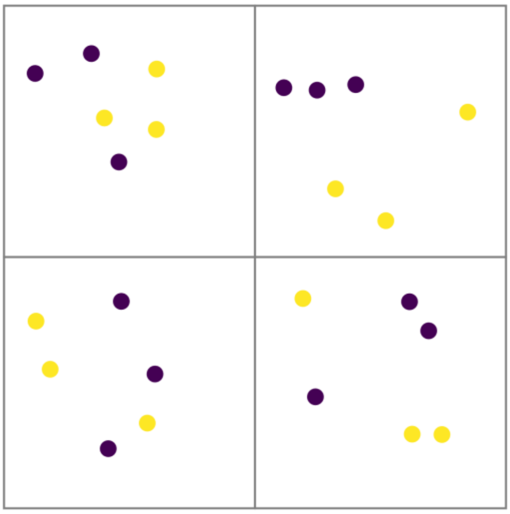

Example 2 – equal distribution, no mixing

The spatial distribution of particles is the same as in example 1 but compositions are not mixed, so S_{pd} is still 1. $P_{j,c}$ is either one or zero per composition which both will lead to a zero for the local entropy which is therefore 0 for all four cells. As this local entropy feeds into the global entropy S, that is also 0.

$$n_{c,j} = \begin{pmatrix} 0 & 0 & 4 & 4 \\ 4 & 4 & 0 & 0 \end{pmatrix}$$

$$N_c = \begin{pmatrix} 2 \\ 2 \end{pmatrix}$$

$$\rho_{c,j} = \begin{pmatrix} 0 & 0 & 2 & 2 \\ 2 & 2 & 0 & 0 \end{pmatrix}$$

$$P_{j,c} = \begin{pmatrix} 0 & 0 & 1 & 1 \\ 1 & 1 & 0 & 0 \end{pmatrix}$$

$$P_j = (1/4 \;\; 1/4 \;\; 1/4 \;\; 1/4)$$

$$S_{pd} = 1.38629$$

$$S_j = (0\ 0\ 0\ 0)$$

$$S = 0$$

$$S_{pd\ normalized} = \frac{1.38629}{\ln 4} = 1$$

$$S_{j\ normalized} = (0\ 0\ 0\ 0)$$

$$S_{normalized} = \frac{0}{\ln 2} = 0$$

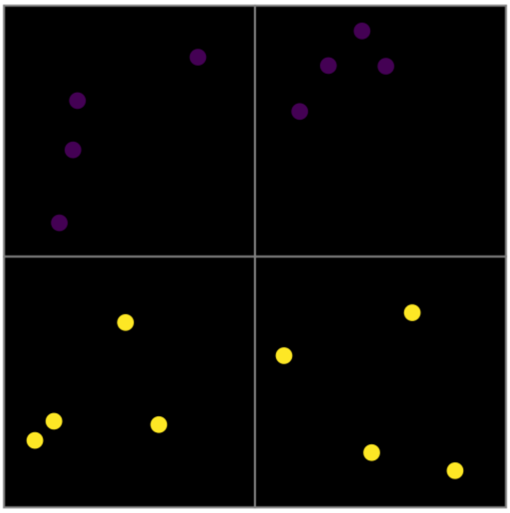

Example 3 – random example with 3 compositions

The distribution is ideally mixed as the expected number of particles in each cell is 3.5. P_j is therefore not the same in each cell, but close to that. S_{pd} is therefore close to 1 in this example. The compositions are not equally distributed, the top left cell is close to the expected distribution (N_c) and therefore has a local entropy close to 1 (after normalization by *ln(3)*). The bottom cells are equally far off expected values (1.5 off for purple, and 1 for the other colors) and have therefore the same S_j. As three cells have local entropy of about 0.5, but distributions are somewhat equal, the global entropy is 0.678 – which reflects the weighted average of S_j which is the global entropy is.

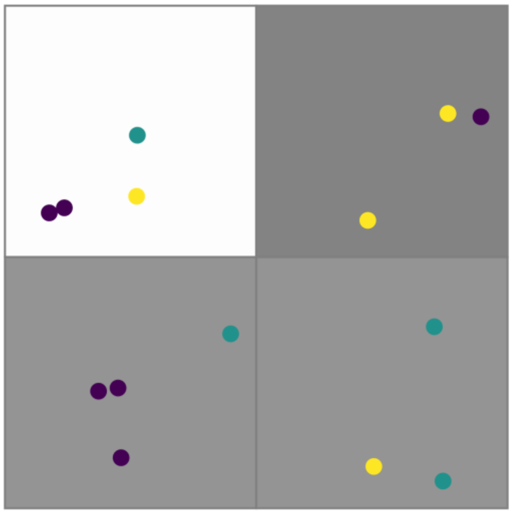

$$n_{c,j} = \begin{pmatrix} 3 & 0 & 2 & 1 \\ 1 & 2 & 1 & 0 \\ 0 & 1 & 1 & 2 \end{pmatrix}$$

$$N_c = \begin{pmatrix} 1.5 \\ 1 \\ 1 \end{pmatrix}$$

$$\rho_{c,j} = \begin{pmatrix} 2 & 0 & {}^{4}/_{3} & {}^{2}/_{3} \\ 1 & 2 & 1 & 0 \\ 0 & 1 & 1 & 2 \end{pmatrix}$$

$$P_{j,c} = \begin{pmatrix} {}^{2}/_{3} & 0 & {}^{4}/_{10} & {}^{1}/_{4} \\ {}^{1}/_{3} & {}^{2}/_{3} & {}^{3}/_{10} & 0 \\ 0 & {}^{1}/_{3} & {}^{3}/_{10} & {}^{3}/_{4} \end{pmatrix}$$

$$P_j = \left({}^{1}/_{4} \ {}^{1}/_{4} \ {}^{5}/_{18} \ {}^{2}/_{9} \right)$$

$$S_{pd} = 1.3832$$

$$S_j = (0.6365 \ \ 0.6365 \ \ 1.0888 \ \ 0.5623)$$

$$S = 0.74569$$

$$S_{pd\ normalized} = \frac{1.38629}{\ln 4} = 0.99777$$

$$S_{j\ normalized} = (0.5794 \ \ 0.5794 \ \ 0.9912 \ \ 0.5119)$$

$$S_{normalized} = \frac{0.74569}{\ln 3} = 0.67876$$

Example 4 – no equal distribution

This last case showcases an uneven particle distribution, with an expected number of particles of 16.75 (sum N_c) that is not recovered in any cell. The vector P_j is therefore not balanced and S_{pd} is 0.689, indicating an imperfect particle distribution. The top left is obviously unmixed with $S_j = 0$. The bottom cells have the same ratio of compositions and therefore a similar high S_j as the 50/50 compositional ratio is not too far off the ideal ratio. The bottom cells contribute significantly to the global entropy S and the top left cell has a sizable weighing factor ($P_3 = 0.238$) but as its $S_j = 0$ it does therefore not contribute to the total entropy.

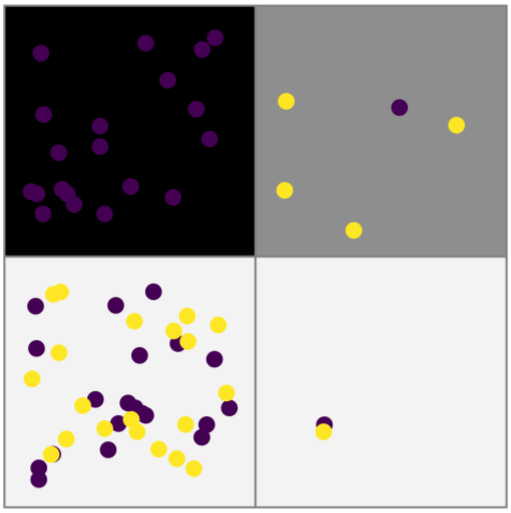

$$n_{c,j} = \begin{pmatrix} 20 & 1 & 20 & 1 \\ 20 & 1 & 0 & 4 \end{pmatrix}$$

$$N_c = \begin{pmatrix} 10.5 \\ 6.25 \end{pmatrix}$$

$$\rho_{c,j} = \begin{pmatrix} 1.9 & 0.095 & 1.905 & 0.095 \\ 3.2 & 0.16 & 0 & 0.64 \end{pmatrix}$$

$$P_{j,c} = \begin{pmatrix} 0.373 & 0.373 & 1 & 0.129 \\ 0.627 & 0.627 & 0 & 0.871 \end{pmatrix}$$

$$P_j = (0.638 \; 0.0319 \; 0.2381 \; 0.0919)$$
$$S_{pd} = 0.9576$$
$$S_j = (0.66 \; 0.66 \;\; 0 \;\; 0.385)$$
$$S = 0.478$$
$$S_{pd\ normalized} = \frac{0.9576}{\ln 4} = 0.6907$$
$$S_{j\ normalized} = (0.953 \;\; 0.953 \;\; 0 \;\; 0.556)$$
$$S_{normalized} = \frac{0.478}{\ln 2} = 0.689$$

Code availability

The code that is used to create the appendix which calculates all the appropriate values can be found online at:

https://github.com/cedrict/fieldstone/blob/master/python_codes/fieldstone_137/ministone.py

Data availability

The data used to make the figures are available on Zenodo (https://zenodo.org/records/10077983)

CRediT authorship contribution statement

EvdW: Conceptualization, Methodology, Investigation, Writing – Original draft, Visualization **CT**: Methodology, Writing – Review & Editing **DJJvH**: Supervision, Writing – Review & Editing

Competing interests

The authors declare that they have no conflict of interest.

Acknowledgements

EvdW and DJJvH acknowledge the support by the Netherlands Organisation for Scientific Research through NWO Vici Grant 865.17.001.

References

Ballmer, M. D., Houser, C., Hernlund, J. W., Wentzcovitch, R. M., & Hirose, K. (2017). Persistence of strong silica-enriched domains in the Earth's lower mantle. *Nature Geoscience, 10*(3), 236-240. https://doi.org/10.1038/NGEO2898

Bower, D. J., Gurnis, M., & Flament, N. (2015). Assimilating lithosphere and slab history in 4-D Earth models. *Physics of the Earth and planetary interiors, 238*, 8-22. https://doi.org/10.1016/j.pepi.2014.10.013

Bull, A. L., Domeier, M., & Torsvik, T. H. (2014). The effect of plate motion history on the longevity of deep mantle heterogeneities. *Earth and Planetary Science Letters, 401*, 172-182. https://doi.org/10.1016/j.epsl.2014.06.008

Camesasca, M., Kaufman, M., & Manas-Zloczower, I. (2006). Quantifying fluid mixing with the Shannon entropy. *Macromolecular theory and simulations, 15*(8), 595-607. https://doi.org/10.1002/mats.200600037

Coltice, N., & Shephard, G. E. (2018). Tectonic predictions with mantle convection models. *Geophysical Journal International, 213*(1), 16-29. https://doi.org/10.1093/gji/ggx531

Dannberg, J., & Gassmöller, R. (2018). Chemical trends in ocean islands explained by plume–slab interaction. *Proceedings of the National Academy of Sciences, 115*(17), 4351-4356. https://doi.org/10.1073/pnas.1714125115

Deschamps, F., Cobden, L., & Tackley, P. J. (2012). The primitive nature of large low shear-wave velocity provinces. *Earth and Planetary Science Letters, 349*, 198-208. https://doi.org/10.1016/j.epsl.2012.07.012

Domeier, M., & Torsvik, T. H. (2014). Plate tectonics in the late Paleozoic. *Geoscience Frontiers, 5*(3), 303-350. https://doi.org/10.1016/j.gsf.2014.01.002

Doucet, L. S., Li, Z.-X., Gamal El Dien, H., Pourteau, A., Murphy, J. B., Collins, W. J., Mattielli, N., Olierook, H. K., Spencer, C. J., & Mitchell, R. N. (2020). Distinct formation history for deep-mantle domains reflected in geochemical differences. *Nature Geoscience, 13*(7), 511-515. https://doi.org/10.1038/s41561-020-0599-9

Dupré, B., & Allègre, C. J. (1983). Pb–Sr isotope variation in Indian Ocean basalts and mixing phenomena. *Nature, 303*(5913), 142-146. https://doi.org/10.1038/303142a0

Faccenna, C., Becker, T. W., Conrad, C. P., & Husson, L. (2013). Mountain building and mantle dynamics. *Tectonics, 32*(1), 80-93. https://doi.org/10.1029/2012TC003176

Flament, N., Bodur, Ö. F., Williams, S. E., & Merdith, A. S. (2022). Assembly of the basal mantle structure beneath Africa. *Nature, 603*(7903), 846-851.

Garnero, E. J., McNamara, A. K., & Shim, S.-H. (2016). Continent-sized anomalous zones with low seismic velocity at the base of Earth's mantle. *Nature Geoscience, 9*(7), 481-489. https://doi.org/10.1038/NGEO2733

Gazel, E., Trela, J., Bizimis, M., Sobolev, A., Batanova, V., Class, C., & Jicha, B. (2018). Long-lived source heterogeneities in the Galapagos mantle plume. *Geochemistry, Geophysics, Geosystems, 19*(8), 2764-2779. https://doi.org/10.1029/2017GC007338

Gerya, T. (2014). Precambrian geodynamics: concepts and models. *Gondwana Research, 25*(2), 442-463. https://doi.org/10.1016/j.gr.2012.11.008

Goltz, C., & Böse, M. (2002). Configurational entropy of critical earthquake populations. *Geophysical Research Letters, 29*(20), 51-51-51-54. https://doi.org/10.1029/2002GL015540

Gülcher, A. J., Gebhardt, D. J., Ballmer, M. D., & Tackley, P. J. (2020). Variable dynamic styles of primordial heterogeneity preservation in the Earth's lower mantle. *Earth and Planetary Science Letters, 536*, 116160. https://doi.org/10.1016/j.epsl.2020.116160

Gülcher, A. J. P., Ballmer, M. D., & Tackley, P. J. (2021). Coupled dynamics and evolution of primordial and recycled heterogeneity in Earth's lower mantle. *Solid Earth, 12*(9), 2087-2107. https://doi.org/10.5194/se-12-2087-2021

Hart, S. R. (1984). A large-scale isotope anomaly in the Southern Hemisphere mantle. *Nature, 309*(5971), 753-757. https://doi.org/10.1038/309753a0

Heister, T., Dannberg, J., Gassmöller, R., & Bangerth, W. (2017). High accuracy mantle convection simulation through modern numerical methods–II: realistic models and problems. *Geophysical Journal International, 210*(2), 833-851. https://doi.org/10.1093/gji/ggx195

Hoernle, K., Werner, R., Morgan, J. P., Garbe-Schönberg, D., Bryce, J., & Mrazek, J. (2000). Existence of complex spatial zonation in the Galápagos plume. *Geology, 28*(5), 435-438. https://doi.org/10.1130/0091-7613(2000)28<435:EOCSZI>2.0.CO;2

Homrighausen, S., Hoernle, K., Hauff, F., Hoyer, P. A., Haase, K. M., Geissler, W. H., & Geldmacher, J. (2023). Evidence for compositionally distinct upper mantle plumelets since the early history of the Tristan-Gough hotspot. *Nature communications, 14*(1), 3908. https://doi.org/10.1038/s41467-023-39585-0

Jackson, M., Becker, T., & Konter, J. (2018). Evidence for a deep mantle source for EM and HIMU domains from integrated geochemical and geophysical constraints. *Earth and Planetary Science Letters, 484*, 154-167. https://doi.org/10.1016/j.epsl.2017.11.052

Jackson, M., Konter, J., & Becker, T. (2017). Primordial helium entrained by the hottest mantle plumes. *Nature, 542*(7641), 340-343. https://doi.org/10.1038/nature21023

Jackson, M., & Macdonald, F. (2022). Hemispheric geochemical dichotomy of the mantle is a legacy of austral supercontinent assembly and onset of deep continental crust subduction. *AGU Advances, 3*(6), e2022AV000664. https://doi.org/10.1029/2022AV000664

Jones, T. D., Sime, N., & van Keken, P. (2021). Burying Earth's primitive mantle in the slab graveyard. *Geochemistry, Geophysics, Geosystems, 22*(3), e2020GC009396. https://doi.org/10.1029/2020GC009396

Koelemeijer, P., Deuss, A., & Ritsema, J. (2017). Density structure of Earth's lowermost mantle from Stoneley mode splitting observations. *Nature communications, 8*(1), 1-10. https://doi.org/10.1038/ncomms15241

Li, Y., Liu, L., Peng, D., Dong, H., & Li, S. (2023). Evaluating tomotectonic plate reconstructions using geodynamic models with data assimilation, the case for North America. *Earth-Science Reviews*, 104518. https://doi.org/10.1016/j.earscirev.2023.104518

Lin, Y. A., Colli, L., & Wu, J. (2022). NW Pacific-Panthalassa intra-oceanic subduction during Mesozoic times from mantle convection and geoid models. *Geochemistry, Geophysics, Geosystems*, e2022GC010514. https://doi.org/10.1029/2022GC010514

McNamara, A. K. (2019). A review of large low shear velocity provinces and ultra low velocity zones. *Tectonophysics, 760*, 199-220. https://doi.org/10.1016/j.tecto.2018.04.015

Merdith, A. S., Williams, S. E., Collins, A. S., Tetley, M. G., Mulder, J. A., Blades, M. L., Young, A., Armistead, S. E., Cannon, J., & Zahirovic, S. (2021). Extending full-plate tectonic models into deep time: Linking the Neoproterozoic and the Phanerozoic. *Earth-Science Reviews, 214*, 103477. https://doi.org/10.1016/j.earscirev.2020.103477

Naliboff, J. B., & Kellogg, L. H. (2007). Can large increases in viscosity and thermal conductivity preserve large-scale heterogeneity in the mantle? *Physics of the Earth and planetary interiors, 161*(1-2), 86-102. https://doi.org/10.1016/j.pepi.2007.01.009

Perugini, D., De Campos, C., Petrelli, M., Morgavi, D., Vetere, F. P., & Dingwell, D. (2015). Quantifying magma mixing with the Shannon entropy: Application to simulations and experiments. *Lithos, 236*, 299-310. https://doi.org/10.1016/j.lithos.2015.09.008

Ritsema, J., Deuss, A., Van Heijst, H., & Woodhouse, J. (2011). S40RTS: a degree-40 shear-velocity model for the mantle from new Rayleigh wave dispersion, teleseismic traveltime and normal-mode splitting function measurements. *Geophysical Journal International, 184*(3), 1223-1236. https://doi.org/10.1111/j.1365-246X.2010.04884.x

Ritsema, J., & Lekić, V. (2020). Heterogeneity of seismic wave velocity in Earth's mantle. *Annual Review of Earth and Planetary Sciences, 48*, 377-401. https://doi.org/10.1146/annurev-earth-082119-065909

Shannon, C. E. (1948). A mathematical theory of communication. *The Bell system technical journal, 27*(3), 379-423. https://doi.org/10.1002/j.1538-7305.1948.tb01338.x

Stracke, A., Genske, F., Berndt, J., & Koornneef, J. M. (2019). Ubiquitous ultra-depleted domains in Earth's mantle. *Nature Geoscience, 12*(10), 851-855. https://doi.org/10.1038/s41561-019-0446-z

Thieulot, C. (2018). Ghost: Geoscientific hollow sphere tessellation. *Solid Earth, 9*(5), 1169-1177. https://doi.org/10.5194/se-9-1169-2018

Van der Meer, D. G., Van Hinsbergen, D. J., & Spakman, W. (2018). Atlas of the underworld: Slab remnants in the mantle, their sinking history, and a new outlook on lower mantle viscosity. *Tectonophysics, 723*, 309-448. https://doi.org/10.1016/j.tecto.2017.10.004

Van der Wiel, E., Van Hinsbergen, D.J.J., Thieulot, C., & Spakman, W. (2023). Linking rates of slab sinking to long-term lower mantle flow and mixing. *Earth and Planetary Science Letters, in press.*

Vilella, K., Bodin, T., Boukaré, C.-E., Deschamps, F., Badro, J., Ballmer, M. D., & Li, Y. (2021). Constraints on the composition and temperature of LLSVPs from seismic properties of lower mantle minerals. *Earth and Planetary Science Letters, 554*, 116685. https://doi.org/10.1016/j.epsl.2020.116685

Weis, D., Garcia, M. O., Rhodes, J. M., Jellinek, M., & Scoates, J. S. (2011). Role of the deep mantle in generating the compositional asymmetry of the Hawaiian mantle plume. *Nature Geoscience, 4*(12), 831-838. https://doi.org/10.1038/ngeo1328

Wellmann, J. F., & Regenauer-Lieb, K. (2012). Uncertainties have a meaning: Information entropy as a quality measure for 3-D geological models. *Tectonophysics, 526*, 207-216. https://doi.org/10.1016/j.tecto.2011.05.001

Wichmann, D., Delandmeter, P., Dijkstra, H. A., & van Sebille, E. (2019). Mixing of passive tracers at the ocean surface and its implications for plastic transport modelling. *Environmental Research Communications, 1*(11), 115001. https://doi.org/10.1088/2515-7620/ab4e77

Yan, J., Ballmer, M. D., & Tackley, P. J. (2020). The evolution and distribution of recycled oceanic crust in the Earth's mantle: Insight from geodynamic models. *Earth and Planetary Science Letters, 537*, 116171. https://doi.org/10.1016/j.epsl.2020.116171

Zahirovic, S., Müller, R. D., Seton, M., & Flament, N. (2015). Tectonic speed limits from plate kinematic reconstructions. *Earth and Planetary Science Letters, 418*, 40-52.